Supramolecular control over the morphology of bio-inspired poly(3-hexylthiophene) for organic thin film transistors

Yen-Ting Lin [a], Ranjodh Singh [a], Shiao-Wei Kuo [b], Fu-Hsiang Ko [a, *]

[a] Department of Materials Science and Engineering, National Chiao Tung University, 1001 University Road, Hsinchu, 30010, Taiwan
[b] Department of Materials and Optoelectronic Science, National Sun Yat-Sen University, No. 70, Lienhai Road, Kaohsiung, 80424, Taiwan

ABSTRACT

We have developed a strategy for modifying the channel layer of organic thin film transistors (OTFTs) through side-chain induced self-organization into a well-ordered film. To obtain selectively self-patterned layers, we treated an adenine-functionalized poly(3-hexylthiophene) (PAT) with adenosine triphosphate (ATP). Using this strategy, interchain charge transport resulting from π-conjugation was selected to control the polymer morphology, without the need of additional chemical synthetic processing. The side chain–induced self-organization can be understood in terms of supramolecular interactions. The π-electrons were delocalized among the thiophene rings, thereby improving the interchain charge transport ability; the resulting planar π-electron system in PAT:ATP resulted in closer intermolecular π–π distances, facilitating enhanced charge carrier mobility within a fibrillar structure. The PAT:ATP-based OTFT device exhibited moderate to improved electronic characteristics, with an average field mobility of 3.2×10^{-4} cm^2 V^{-1} s^{-1} at -30 V and a threshold voltage (V_{th}) of 5 V, and an on/off current ratio of 10^6. This method has great potential for inducing selective intermolecular interactions in fully solution processed electronic devices.

© 2016 Elsevier B.V. All rights reserved.

1. Introduction

In addition to their synthesis, the structure property relationships of new conjugated polymers and their characteristics on the nanometer scale are being explored extensively for potential uses in emerging advanced technological applications, including polymer light-emitting diodes [1], polymer solar cells [2], and organic thin-film transistors (OTFTs) [3]. The electrical performance of these devices is dictated by the morphology of the conjugated polymers commonly employed within them, especially in the case of OTFTs. The mobility of charge carriers in conjugated polymer–based OTFT is dependent on the annealing temperature [4] and the solvent and concentration used for processing [5]. Because of good solubility in organic solvents and relatively high field-effect mobility in the solid state, the morphologies of thin films formed from conjugated polymers can be controlled efficiently through modification of the noncovalent interactions between their polymer chains [5,6]. These noncovalent interactions can change the morphology of the as-formed thin film when applied as a channel layer, a process occurring through self-assembly mediated through van der Waals, hydrogen bonding, and π-stacking interactions [7,8]. These noncovalent interactions are all driving forces affecting self-assembly of poly(3-hexylthiophene) (P3HT) in organic solvents and in the solid state [9,10].

Carrier mobility is the one of most important factors directly governing the performance of semiconductor devices. P3HT has been the most intensively studied semiconducting polymer for OTFTs; it is used widely as a channel layer because of its relatively high field-effect mobility (0.1–0.3 cm^2 V^{-1} s^{-1}), which is close to the value for an amorphous silicon film [11–13]. Thus, controlling the morphology of P3HT can be an effective strategy for enhancing the electronic performance of its OTFT devices. For example, blending some distinctive materials with P3HT may affect its crystallinity, potentially leading to greater stability and a preferential orientational alignment in a semi-crystalline polymer film and, thereby, improving charge carrier mobility through the otherwise soft backbone of P3HT [14]. Accordingly, developing new methods for the deposition of semiconductor thin films through solution-processing should allow their efficient self-assembly and organization into higher degrees of molecular ordering. Some studies have been performed to determine the structure–mobility relationships of P3HT. Liu et al. reported that the mobility of a

* Corresponding author.
  E-mail address: fhko@mail.nctu.edu.tw (F.-H. Ko).

conjugated polymer is limited by its interconnected network and nanoscale aggregates [15]. It would be interesting to determine whether the patterns of interaction strategies and strengths would be retained or improved upon in a hybrid material used as a channel layer in OTFTs [16]. From research into P3HT-based composite films, improving the functional performance of P3HT hybrid materials and enhancing the carrier mobility of P3HT may increase its applications. Most existing research agrees that the properties of P3HT are determined by its phase of aggregation and morphology [17]; therefore, various methods have been tested to improve the carrier mobility of P3HT by controlling its self-assembly in polymer films, including choosing an appropriate solvent [18], modifying P3HT with various functional groups [19], and optimize its annealing conditions [20]. All of these approaches have had the goal of improving the crystallinity of the conjugated polymer and optimizing the orientation of its polymer chains in a preferred direction [21,22].

In this paper we report a new method, based on supramolecular chemistry, for controlling the morphology of films formed from an adenine-functionalized polythiophene (PAT) and its application in OTFTs. The performance of these electronic devices was dependent on the morphology of PAT applied as a channel layer within them. Indeed, the morphology of the PAT channel layer could be controlled through the blending of PAT with adenosine triphosphate (ATP). When applied in OTFTs, this new hybrid supramolecular channel layer resulted in enhanced electric performance. We have used Fourier transform infrared (FTIR) spectroscopy, atomic force microscopy (AFM), transmission electron microscopy (TEM), and UV spectroscopy to explore the morphologies of these blended channel layers. These studies have revealed that the performance of the resulting OTFTs was controlled through variations in the degree of adenine–adenine (A···A) hydrogen bonding.

2. Experimental

2.1. Materials

Bromoacetic acid methyl ester, uracil, and 1,3-propanediamine were purchased from Alfa–Aesar. 3-Bromothiophene, 1,6-dibromohexane, anhydrous iron(III) chloride, adenosine 5′-triphosphate disodium salt hydrate (ATP, ≥99%), and anhydrous chloroform were purchased from Sigma–Aldrich. Tetrahydrofuran and dimethylformamide were heated under reflux over CaH_2 under a N_2 atmosphere and distilled prior to their use. All other reagents and anhydrous solvents were obtained from local suppliers without further purification, unless otherwise noted.

2.2. Characterization

^{1}H and ^{13}C NMR spectra were recorded at 300 and 75 MHz, respectively, using a Bruker DPX-300S spectrometer equipped with a 9.395-T Bruker magnet. The samples (ca. 7 mg for ^{1}H NMR; ca. 25 mg for ^{13}C NMR) were dissolved in deuterated solvents and analyzed at room temperature. Differential scanning calorimetry (DSC) was performed using a DuPont 910 DSC-9000 controller operated under a dry N_2 atmosphere. The samples were weighed (ca. 8–10 mg) and sealed in an aluminum pan, then heated from 0 to 100 °C at a scan rate of 20 °C min^{-1}. The glass transition temperature was taken as the midpoint of the heat capacity transition between the upper and lower points of the deviation from the extrapolated glass and liquid lines. Thermogravimetric analysis (TGA) was performed using a TA Instruments TGA 2050 analyzer operated at a heating rate of 20 °C min^{-1} from room temperature to 800 °C under a continuous flow of N_2. FTIR spectra were recorded using a Nicolet Avatar 320 FTIR spectrometer; 32 scans were

collected at a spectral resolution of 1 cm^{-1}. The conventional KBr pellet and Si substrate methods were employed; the sample was dissolved in tetrachloroethane and then cast onto a KBr pellet. UV–Vis and photoluminescence (PL) spectra were measured using an HP 8453 diode-array spectrophotometer and a Hitachi F-4500 luminescence spectrometer, respectively. The samples sputtered with TEM images were obtained using a Hitachi HT7700 instrument operated at 120 kV; the samples were dip-coated from a freshly made solution onto a carbon-coated copper grid. AFM images were recorded at room temperature using a NanoScope IIIa AFM (Digital Instrument, EnviroScope).

2.3. Synthesis of 3-(Adeninehexyl)thiophene

In Scheme 1, a solution of 3-bromothiopene (a, 30.0 g, 0.180 mol) in n-hexane (250 mL) was cooled to −40 °C. n-BuLi was injected into this solution and the resulting mixture stirred for 10 min. Dry THF (15–20 mL) was added slowly dropwise from a syringe until an insoluble white precipitate (3-lithiothiophene salt) had formed. The temperature was increased from −40 to −10 °C and then the mixture was stirred for 1 h. A solution of 1,6-dibromohexane (b, 110 mL, 0.720 mol) in THF (5–10 mL) was added dropwise into this mixture over 2 h at room temperature with continuous stirring. After completion of the reaction, the mixture was washed sequentially with ether and water. Rotary evaporation of the organic phase provided a colorless oily residue (c, 27.4 g, 68%). A portion of this residue (c, 2.79 g, 20.0 mmol), calcium carbonate (5.58 g, 40.0 mmol), and adenine (5.40 g, 40 mmol) were placed in dry DMF (200 mL) and then the mixture was stirred at 60 °C for 24 g. When the reaction was complete, the mixture was cooled to room temperature, filtered to remove any insoluble solids, and concentrated under low-pressure distillation. The residue was recrystallized (toluene) to give 3-(adeninehexyl)thiophene (d, 5.00 g, 45%). The monomer structure was confirmed spectroscopically: ^{1}H NMR (300 MHz, CDCl$_3$) δ = 1.34–1.36 (m, 4H), 1.65 (br, 2H), 2.60–2.62 (m, 2H), 3.68 (t, 2H), 5.65 (d, 1H), 6.89 (d, 1H), 7.08 (d, 1H), 7.21 (d, 1H), 8.80 (s, ^{1}H) ppm; ^{13}C NMR (75 MHz, CDCl$_3$) δ = 26.45, 28.96, 29.19, 30.30, 30.49, 49.06, 102.34, 120.17, 125.45, 128.40, 142.96, 144.65, 151.15, 164.18 ppm (Fig. S1).

2.4. Synthesis of poly(3-(Adeninehexyl)thiophene)

A 250-mL double-neck round-bottom flask was placed in a cooling bath and charged with FeCl$_3$ (4.00 g, 137 mol) in dehumidified air under an Ar atmosphere. A small amount of dry CHCl$_3$ was added to this assembly to dissolve the FeCl$_3$, then a solution of 3-(adeninehexyl)thiophene (d, 1.73 g, 5.74 mmol, see Scheme 1) in dry CHCl$_3$ (20 mL) was added dropwise. The reaction was allowed to proceed for several days to ensure complete polymerization. At that point, the CHCl$_3$ was evaporated through low-pressure distillation and then MeOH was added to precipitate the polymer (PAT). The crude polymer was washed with a small amount of hydrazine. Further purification through Soxhlet extraction and removal of MeOH provided PAT (68%). ^{1}H NMR (400 MHz, DMSO-d_6): δ = 1.20–1.22 (m, 4H), 1.53–1.54 (m, 2H), 1.71–1.72 (m, 2H), 2.65 (t, 2H), 4.05 (t, 2H), 7.07 (s, 1H), 7.20 (s, 2H), 8.08 (s, 2H) (Fig. S2). IR (KBr): 3250, 2835, 1615, 520, 710 cm^{-1} (Fig. S3). MS (EI), [M$^+$]: m/z 2840; calculated: 2840.68 (Fig. S4).

2.5. PAT:ATP hybrid

PAT and ATP (10 mg/10 mg) were blended in dimethyl sulfoxide (DMSO, 1 mL) at 80 °C for 24 h. This warm mixture was filtered through a 0.45-μm PALL, 13-mm PTFE membrane to yield the target nanocomposite material for further use. The solution was
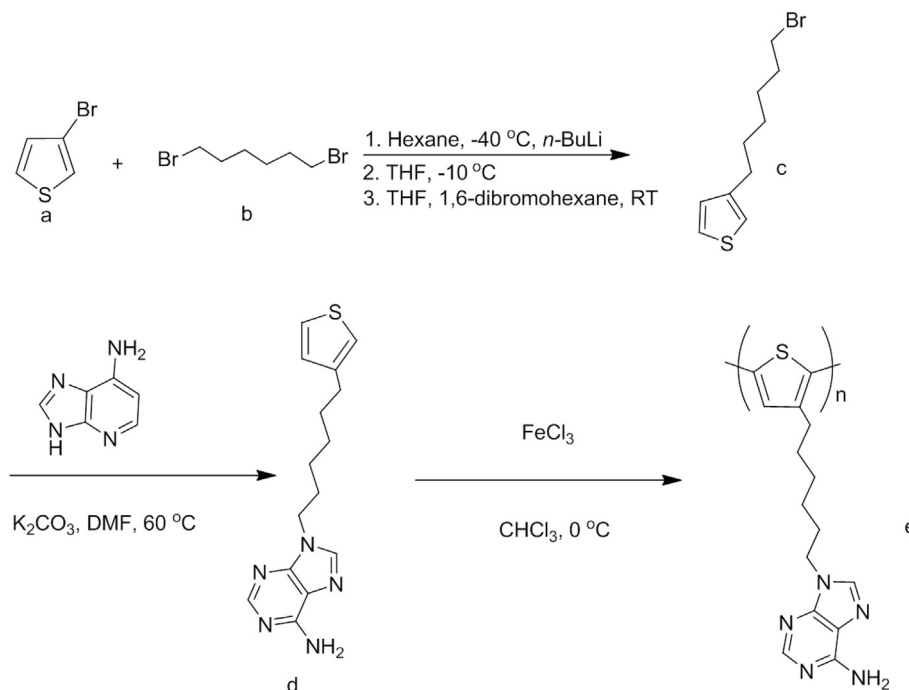
Scheme 1. Synthesis of PAT.

centrifuged (4000 rpm, 1 min) in a Digisystem DSCN 158A rotor. The supernatant, the homogeneous PAT:ATP solution, was collected for further study [9].

2.6. OTFT devices

An *n*-type Si substrate was cleaned with EtOH (Fluka; water content: <0.1%) through ultrasonication (30 min) and soaking in deionized water for 10 min, followed by treatment with a high-pressure N₂ air gun purge to remove the water and any remaining surface particles on it. After cleaning, the Si substrate was dried in oven at 200 °C for 10 min to remove any moisture from its surface. A 50-nm-thick layer of Al was deposited on the Si substrate as a bottom electrode. A 200-nm-thick SiO₂ dielectric layer was the deposited over the Si substrate. To deposit the channel layer, a sol−gel solution was prepared by using DMSO (1 mL) and the PAT solution (10 mg) and the PAT-ATP (10/10 mg) solution. These solutions were stirred at room temperature for 24 h, resulting in a brown dark and brown mixed solution, respectively. The dielectric layers were deposited through spin-coating of the solutions over the Si substrate at 800 rpm for 20 s and 1600 rpm for 20 s, respectively, at room temperature, using a homemade spin-coater. Typically, the PAT layer was spin-coated three times, and the PAT-ATP layer was spin-coated three times over it. After depositing the dielectric layer, annealing of the layers was performed at 130 °C for 30 min; a custom shadow mask was then applied to deposit 120-nm-thick Al as the top electrode. Finally, source (S) and drain (D) of Al electrodes (thickness: 120 nm) were deposited through a shadow mask to give Al/Si/SiO₂/PAT/Al and Al/Si/SiO₂/PAT-ATP/Al device configurations (i.e., bottom-contact, top-electrode OTFTs). The channel length (*L*) and width (*W*) were 80 and 2300 μm, respectively.

2.7. Electrical characteristics of OTFT devices

The electrical characteristics of the transistors were measured in a N₂ glove box of an Agilent-4156 probe station. The transistor parameters (e.g., charge carrier mobility) were calculated using the standard formalism of field-effect transistors in the linear regime. The PAT-based OTFTs exhibited output characteristics with pinch-off and current saturation. The electrical characteristics of the PAT-based OTFTs remained very stable during operation.

$$I_{DS} = \frac{WC_i}{L}\mu_{FE} \ (V_G - \ V_{th})V_{DS} \tag{1}$$

Here, *W* and *L* denote the S−D width and length, respectively; μ_{FE} is the field effect mobility; C_i is the capacitance per unit area of the insulator; V_{th} is the threshold voltage; and I_{DS} and V_{DS} are the current and voltage bias between the S and D. Thus, the value of μ_{FE} in the linear region (μ_{FE}, lin) could be obtained from the transfer characteristics using Eq. (1). The average field-effect mobility of the PAT transistor in the linear regime was calculated by plotting the square root of the drain current with respect to the voltage [16].

3. Results and discussion

The adenine molecule can self-assemble into network structures because it presents both hydrogen bond donor and acceptor units. We explored this property of adenine in a previous study for its application in flexible memory devices [9]. We found that micelle formation was controlled with substitution of adenine over PAT, allowing the creation of its own stable micelles and reversed micelles with [6,6]-phenyl-C₆₁-butyric acid methyl ester in organic solvents of diverse polarity [8]. These intriguing results motivated us to further explore the morphology of PAT for its possible applications in organic electronic devices. Accordingly, in this present study we synthesized PAT:ATP nanocomposite materials. For primary structure analysis of this new hybrid structure, we used transmission FTIR spectroscopy (Fig. 1). We attribute the bands at 960 and 1015 cm⁻¹ to symmetric and asymmetric P−O stretching, respectively, of the ATP units [23], confirming that the ATP molecules had been attached successfully to PAT. The absorption bands
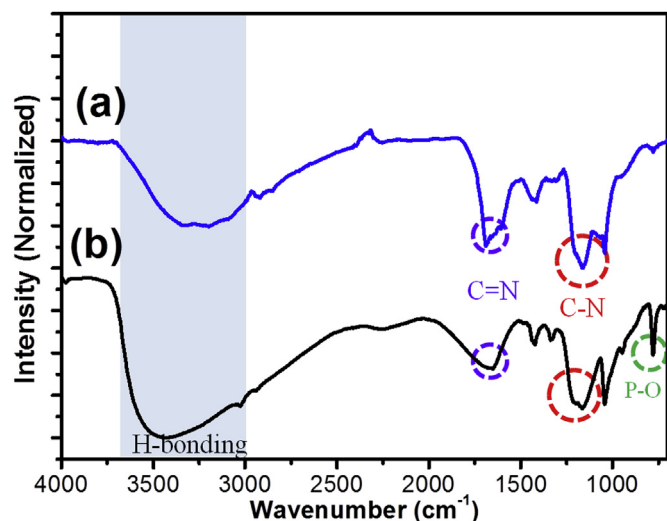
Fig. 1. FTIR spectra of (a) spherical PAT and (b) fibrillar PAT:ATP, with chemical bonds depicting their hydrogen bonding interactions.

at 1165 and 1685 cm^{-1} represent the C—N and C=N bonds, respectively, that were present in the adenine structure and in PAT and ATP. The FTIR spectrum of PAT features a broad band near 3352 cm^{-1}, which represents N—H bonds; this signal shifted to 3465 cm^{-1} in the FTIR spectrum of PAT:ATP. This shift resulted from the interaction of the adenine units of PAT with the ATP units. The FTIR spectroscopic study confirmed the existence of multiple hydrogen bonding interactions between the PAT and ATP groups in the PAT:ATP nanocomposite [24].

After substitution of hydrogen bonding groups on P3HT, it became amorphous, because of this, we employed tapping-mode AFM and TEM study to explore how these various noncovalent interactions affected the morphology of the PAT:ATP nanocomposite material. The charge mobility of an organic semiconductor material is greatly influenced by its microstructure [25]. Hence, we wished to explore the morphology of the PAT:ATP nanocomposite before employing it as a charge transport layer in OTFTs, thereby allowing us to correlate its charge-transport properties with its surface morphology. The AFM images in Fig. 2a and b reveal a clear change in morphology of PAT from a spherical architecture, with small and uniform domain sizes, to a fibrillar architecture after the addition of ATP. In other words, the addition of ATP to the PAT polymer resulted in the spherical domains of PAT polymer to open up and form a fibrillar structure (PAT:ATP) in which the polymer chains stacked together. Fig. 2b presents the AFM image of a PAT:ATP nanocomposite in which we can clearly observe this fibrillar structure. The PAT:ATP fibrillar structure was interconnected through the ATP units, stabilized through intermolecular adenine—adenine (A⋯A) hydrogen bonding (Fig. 2c) [26]. The FTIR spectra had already revealed the existence of these hydrogen bonds between the adenine unit of ATP and the adenine unit of PAT. Fig. 2d and e (Fig. S6) display TEM images of the PAT and PAT:ATP samples, respectively. The TEM image of the PAT sample also reveals its spherical structure. Again, a change in morphology from a spherical to fibrillar structure was evident upon the addition of ATP to PAT to form the PAT:ATP nanocomposite.

The AFM topographic and TEM images revealed that the morphology of PAT changed from spherical architectures to a fibrillar one after the addition of ATP. We used thermogravimetric analysis to further explore the opened up structure of the PAT:ATP nanocomposite. Fig. 3 presents TGA traces of the PAT:ATP nanocomposite and the PAT polymer. Because of its opened up structure,

the PAT:ATP nanocomposite was less resistant to heat when compared with the spherical architecture of PAT. Indeed, the decomposition temperature (T_d) for the PAT polymer (350 °C) was considerably higher than that for the PAT:ATP nanocomposite (<200 °C). This finding gives further evidence, from another perspective, for the existence of intermolecular A⋯A hydrogen bonding in the PAT:ATP nanocomposite [27]. The fibrous weak structure of PAT:ATP featured PAT polymer chains in opened up configuration with crosslinking through A⋯A hydrogen bonds, whereas the pristine PAT polymer existed as aggregates having a spherical architecture because of strong intramolecular A⋯A hydrogen bonding. The disruption of the intramolecular A⋯A hydrogen bonds was necessary to overcome the aggregated architecture of the PAT polymer and allow it to be employed as the channel layer in OTFTs, because the aggregated forms of π-conjugated polymers have low charge transport. Accordingly, we used UV−Vis spectroscopy to further study this phenomenon [28].

Fig. 4 displays the UV absorption spectra of the PAT polymer and the PAT:ATP composite. We suggest that the main absorption arose from the P3HT molecules, with the disruption in A⋯A hydrogen bonding and π-stacking of the PAT polymer, upon the addition of ATP, leading to the formation of PAT:ATP [29]. Evidence for the formation of this nanocomposite can be seen in Fig. 4. The absorption band for PAT:ATP was slightly blue-shifted relative to that of the PAT solution, indicative of compact packing phenomenon between ATP molecules through intermolecular hydrogen bonds [30]. Furthermore, the absorption spectrum of PAT:ATP indicates that the quenching likely arose from conformational change from regioregular crystalline P3HT rather than from surface disruption [31]. Through this strategy, the morphological change caused by π-conjugation could be selected to control the polymer morphology without requiring a chemical synthetic process. The increase in π-stacking may have arisen in the form of a greater population of crystalline aggregates or longer crystalline aggregates generated, as in the case of PAT:ATP [32]. The increased number of π-interactions of P3HT would result in improved charge mobility and, thereby, improved performance of its OTFTs, with a consequent improvement in the efficiency of the $I-V$ curve.

To study the potential of using PAT:ATP as a channel layer, we fabricated PAT:ATP-based bottom-gate/top-contact OTFTs, with a channel width of 2000 μm and a channel length of 82 μm (Fig. 5b) [16]. Fig. 5a presents a photographic image of OTFTs fabricated on an *n*-type Si substrate, with its corresponding configuration depicted in Fig. 5b. Fig. 5c provides the transfer characteristics of the OTFTs. Fig. 5d displays the drain current−drain voltage ($I_{DS}-V_{DS}$) output curve obtained from our OTFT having a 200-nm-thick SiO$_2$ dielectric layer (C_i = 1.73 × 10^{-8} F m^{-1}). The device demonstrated desirable OTFT characteristics, with an operating voltage of less than −30 V and a maximum saturation current of 0.80 mA. The observed OTFT characteristics aligned closely to conventional transistor models in both the linear and saturation regimes, with the value of I_{DS} increasing linearly at low drainage voltage and clear saturation behavior at high drain voltage [33,34]. According to the drain current−gate voltage ($I_{DS}-V_{GS}$) transfer curve in Fig. 5c, the PAT:ATP-based OTFTs having a SiO$_2$ dielectric layer displayed an average field mobility of 3.2 × 10^{-4} cm^2 V^{-1} s^{-1} at −30 V, a threshold voltage (V_{th}) of 5 V, and an on/off current ratio of 10^6.

To explore the relationship between morphology and mobility, we performed AFM analysis of the corresponding morphologies of thin films of PAT and PAT:ATP. Fig. 6 demonstrates their respective AFM images and are recorded in topographic mode. Fig. 6a reveals that the PAT polymer formed an aggregated architecture, in which charges would be retained within deep traps [35]. Hence, the charge carriers would not be able to hop—the common charge
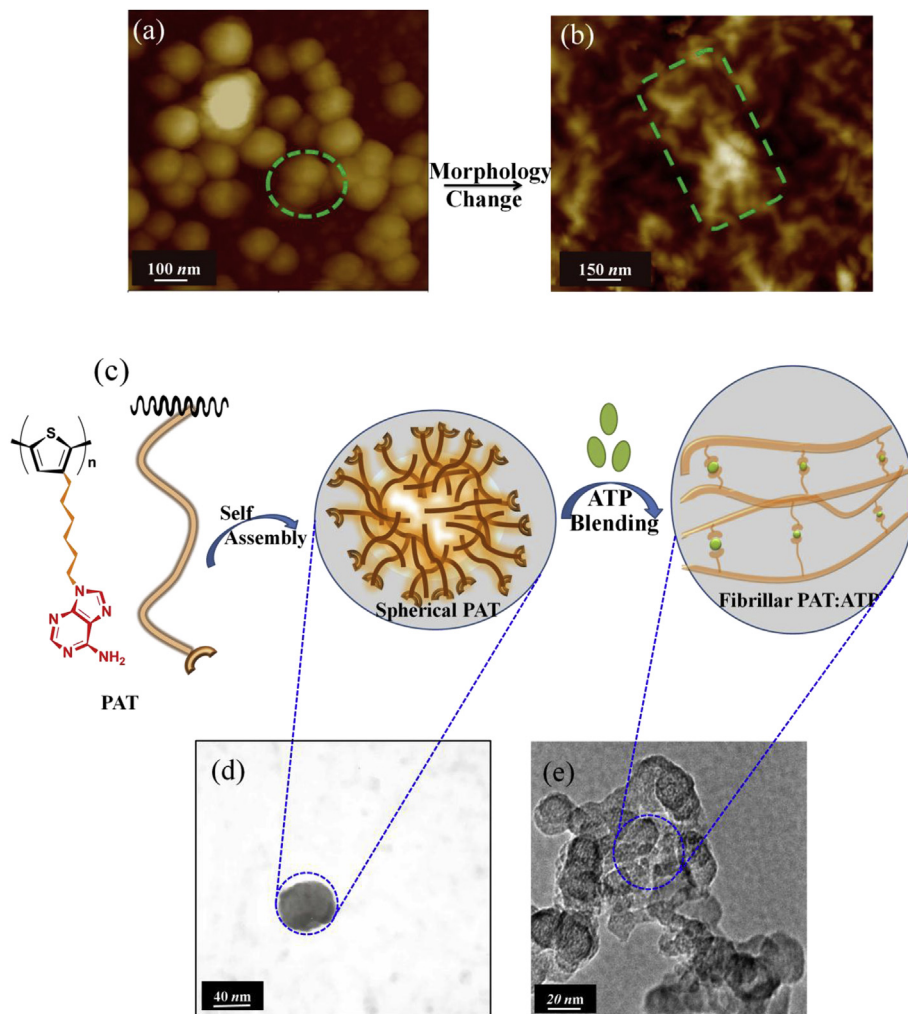
Fig. 2. Topographic AFM images of (a) PAT and (b) PAT:ATP nanocomposite. (c) Schematic representation of the mechanism of the morphological change of the PAT polymer, as triggered by ATP, TEM images of (d) PAT and (e) PAT:ATP.

transport mechanism in OTFTs—in this spherical structure [36,37]. The drain current−gate voltage (I_{DS}−V_{GS}) transfer characteristics (Fig. S7, Supplementary Information) of PAT arose from the non-

switchable behavior of OTFTs based on it. Thus, PAT alone does not have the potential to function as a good charge transport material. After blending with ATP, however, switchable behavior was
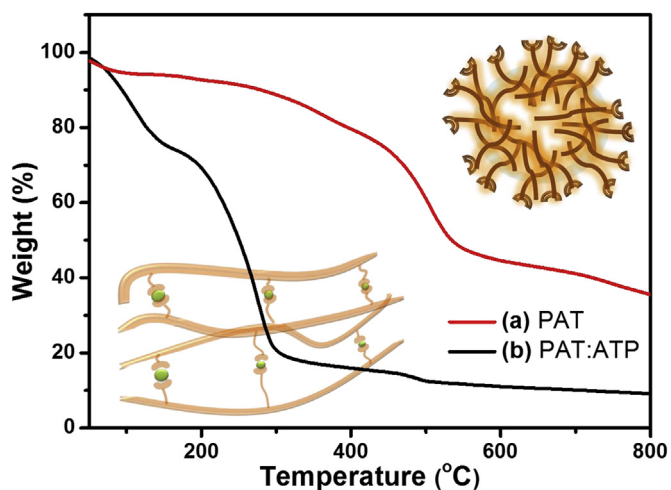

Fig. 3. TGA thermograms for (a) PAT and (b) PAT:ATP, from 30 to 800 °C, measured under N₂.
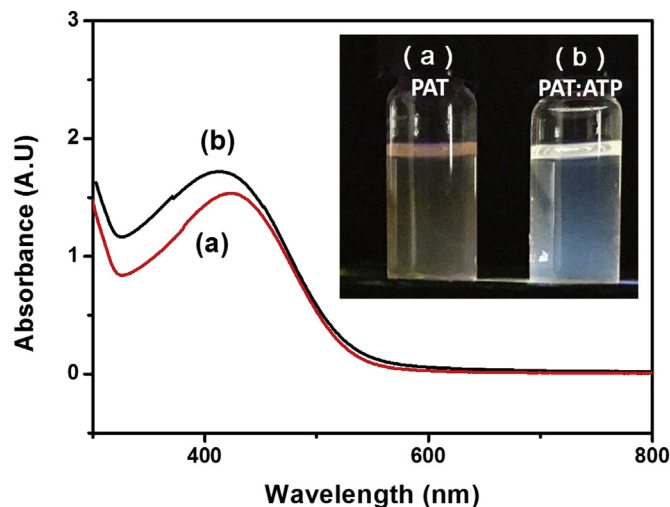
Fig. 4. UV−Vis spectra of (a) PAT and (b) PAT:ATP, each at a concentration of 0.25 wt% in DMSO. Inset photograph: photo images for PAT and PAT:ATP under uv light.
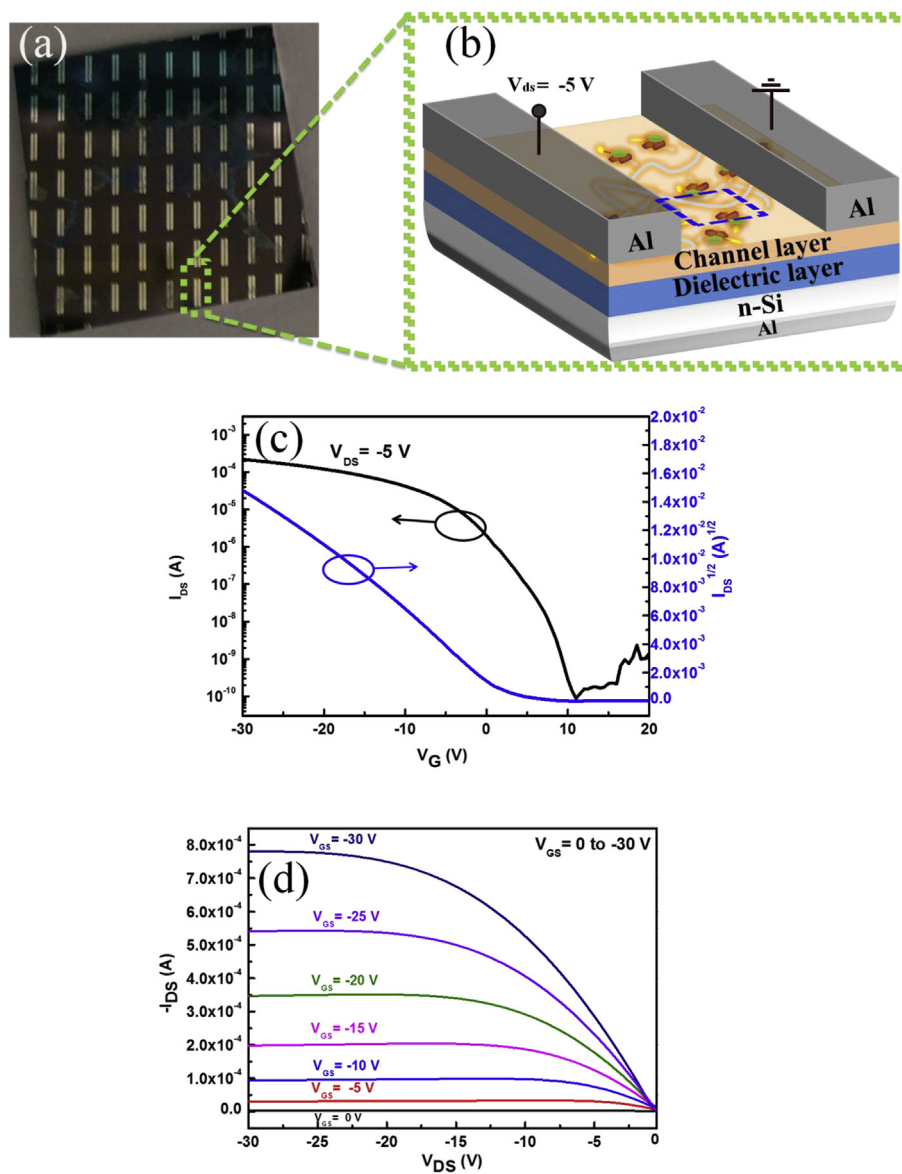
Fig. 5. (a) Photographic image of bottom-gate, top-contact OTFTs. (b) Schematic representation of the structure of a bottom-gate, top-contact OTFT device featuring SiO_2 as a gate insulator and PAT:ATP as a semiconducting layer. (c) (I_{DS}—V_{GS}) and its mobility characteristic for PAT:ATP at V_{DS} of −2.5 V (d) Output characteristic (I_{DS}—V_{DS}) for PAT:ATP, with V_{GS} varied from 0 to −30 V in steps of −5 V.
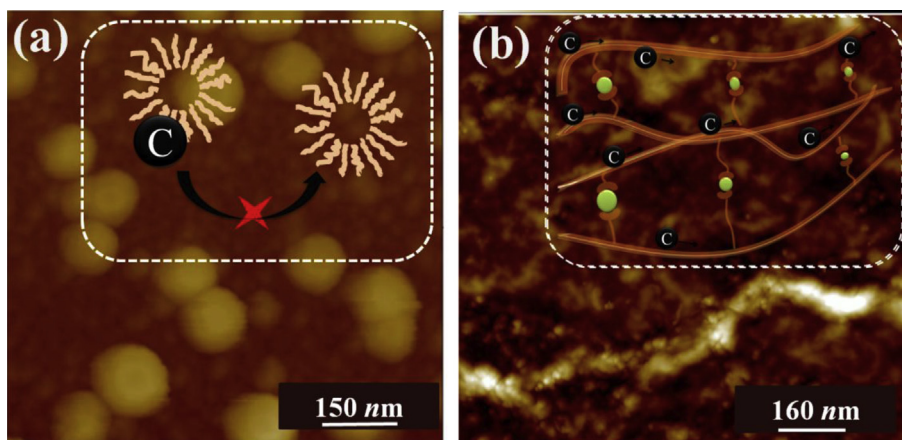
Fig. 6. AFM images of (a) spherical PAT (inset: charge does not hop between thiophene rings in its spherical morphology) and (b) PAT:ATP, revealing side chain—induced self-organization in its fibrillar structure (inset: schematic representation of interchain charge transport).

Table 1
The compared results of the mobility in polythiophene based OTFTs.

Molecules	Mobility ($cm^2 V^{-1} s^{-1}$)	Vth (V)	Morphology	Ref
RR-P3HT	3.0×10^{-4}		Crystalline/CHCl$_3$	[42]
RR-P3HT	5.0×10^{-4}		Crystalline/xylene	[43]
P3HT/ZnO	6.7×10^{-5}	40	Porous	[44]
P3HT/SDS	9.0×10^{-5}	−6.7	Colloid	[45]
P3HT/SDBS	1.7×10^{-4}	5.5	Colloid	[45]
P3HT/DOBS	1.1×10^{-3}	−2.6	Colloid	[45]
PAT/ATP	3.2×10^{-4}	5	Fibrillar	

Noted: RR-P3HT is abbreviated to RegioRegular-P3HT, SDS is abbreviated to sodium dodecyl sulfate, SDBS is abbreviated to sodium dodecylbenzenesulfoante, DOBS is abbreviated to Disodium 4-dodecyl-2,4 −oxydibenzenesulfonate.

obtained because of side chain−induced self-organization into a well-ordered one-dimensional fibrillar structure (Fig. 6b) [38], This transformation released the steric strain from the proximal side chains of the PAT polymer and resulted in the PAT:ATP composite polymer existing in the fibrillar morphology depicted in Fig. 6b [39,40]. In this morphology, the π-electrons were delocalized between the thiophene rings, thereby improving the interchain charge transport ability. Furthermore, the planar π-electron system in PAT:ATP narrowed the intermolecular π−π distances [41], thereby facilitating charge carrier mobility. However, the value of mobilities and their morphology for polythiophene backbone polymers coated from solution were shown in Table 1, the hole mobilities based on colloids are relatively lower. The closed gathering particles still have discrete contact area, due to hole trapped between the boundaries of colloids. In P3HT/ZnO, it suggesting that Frenkel-Poole conduction is dominated if there is a high density of traps in its porous morphology under the high voltage biases.

4. Conclusions

We have prepared a *p*-channel OTFT having a hole mobility of $3.2 \times 10^{-4} cm^2 V^{-1} s^{-1}$ at −30 V. The charge mobility was strongly dependent on the film morphology. We have developed an alternative technique to improve the mobility of adenine-functionalized P3HT without chemical treatment; the resulting films self-organized into channel layers with well-defined feature shapes. Such side chain−induced self-organization arose from a combination of intermolecular hydrogen bonding and π-stacking interactions. Various analyses revealed that the PAT:ATP-based self-patterned OTFT devices exhibited moderate to slightly improved electronic characteristics.

Appendix A. Supplementary data

Supplementary data related to this article can be found at http://dx.doi.org/10.1016/j.orgel.2016.11.008.

References

[1] Y.-L. Chu, C.-C. Cheng, Y.-P. Chen, Y.-C. Yen, F.-C. Chang, A new supramolecular POSS electroluminescent material, J. Mater. Chem. 22 (2012) 9285−9292.
[2] F. Padinger, R.S. Rittberger, N.S. Sariciftci, Effects of postproduction treatment on plastic solar cells, Adv. Funct. Mater. 13 (2003) 85−88.

[3] Y. Chen, G. Xie, T. Xie, Y. Liu, H. Du, Y. Su, Y. Jiang, Thin film transistors based on poly (3-hexylthiophene)/[6, 6]-phenyl C 61 butyric acid methyl ester hetero-junction for ammonia detection, Chem. Phys. Lett. 638 (2015) 87−93.
[4] W. Tang, M. Helander, J. Qiu, M. Greiner, Z. Lu, W. Ng, Thermal annealing effect on electrical characteristics of CuPc thin-film transistors on glass with ZrO 2 as gate dielectric, electron devices and solid-state circuits (EDSSC), in: IEEE International Conference on, IEEE2015, 2015, pp. 197−200.
[5] J.A. Reinspach, Y. Diao, G. Giri, T. Sachse, K. England, Y. Zhou, C. Tassone, B.J. Worfolk, M. Presselt, M.F. Toney, Tuning the morphology of solution-sheared P3HT: PCBM films, ACS Appl. Mater. Inter 8 (2016) 1742−1751.
[6] P. Roy, A. Jha, J. Dasgupta, Photoinduced charge generation rates in soluble P3HT: PCBM nano-aggregates predict the solvent-dependent film morphology, Nanoscale 8 (2016) 2768−2777.
[7] H.-C. Liao, C.-S. Tsao, Y.-C. Huang, M.-H. Jao, K.-Y. Tien, C.-M. Chuang, C.-Y. Chen, C.-J. Su, U.-S. Jeng, Y.-F. Chen, Insights into solvent vapor annealing on the performance of bulk heterojunction solar cells by a quantitative nano-morphology study, RSC Adv. 4 (2014) 6246−6253.
[8] S.-i. Yusa, M. Kamachi, Y. Morishima, Self-association of cholesterol-end-capped poly (sodium 2-(acrylamido)-2-methylpropanesulfonate) in aqueous solution, Macromolecules 33 (2000) 1224−1231.
[9] C.-C. Cheng, F.-C. Chang, F.-H. Ko, F.-C. Yu, Y.-T. Lin, Y.-T. Shieh, J.-K. Chen, D.-J. Lee, Supramolecular polymeric micelles as high performance electro-chemical materials, J. Mater. Chem. C 3 (2015) 9528−9533.
[10] A.P. Schenning, E. Meijer, Supramolecular electronics; nanowires from self-assembled π-conjugated systems, Chem. Comm. (2005) 3245−3258.
[11] S.Y. Son, Y. Kim, J. Lee, G.-Y. Lee, W.-T. Park, Y.-Y. Noh, C.E. Park, T. Park, High field-effect mobility of low-crystallinity conjugated polymers with localized aggregates, J. Am. Chem. Soc. 138 (2016) 8096−8103.
[12] M.J. Ford, M. Wang, S.N. Patel, H. Phan, R.A. Segalman, T.-Q. Nguyen, G.C. Bazan, High Mobility Organic field-effect transistors from majority insulator blends, Chem. Mater. 28 (2016) 1256−1260.
[13] H. Luo, C. Yu, Z. Liu, G. Zhang, H. Geng, Y. Yi, K. Broch, Y. Hu, A. Sadhanala, L. Jiang, Remarkable enhancement of charge carrier mobility of conjugated polymer field-effect transistors upon incorporating an ionic additive, Sci. Adv. 2 (2016) e1600076.
[14] J.I. Scott, X. Xue, M. Wang, R.J. Kline, B.C. Hoffman, D.B. Dougherty, C. Zhou, G.C. Bazan, B.T. O'Connor, Significantly increasing the ductility of high performance polymer semiconductors though polymer blending, ACS Appl. Mater. Inter 8 (2016) 14037−14045.
[15] S. Liu, P. Gordiichuk, Z.-S. Wu, Z. Liu, W. Wei, M. Wagner, N. Mohamed-Noriega, D. Wu, Y. Mai, A. Herrmann, Patterning two-dimensional free-standing surfaces with mesoporous conducting polymers, Nat. Comm. 6 (2015) 8817.
[16] R. Singh, J.S. Meena, I.-H. Tsai, Y.-T. Lin, C.-J. Wang, F.-H. Ko, Solution processable bilayered gate dielectric towards flexible organic thin film transistors, Org. Electron 19 (2015) 120−130.
[17] W. Zhou, J. Shi, L. Lv, L. Chen, Y. Chen, A mechanistic investigation of morphology evolution in P3HT−PCBM films induced by liquid crystalline molecules under external electric field, Phys. Chem. Chem. Phys. 17 (2015) 387−397.
[18] G. Xiao, Y. Sun, W. Xu, Y. Lin, Z. Su, Q. Wang, Large-scale highly ordered hierarchical structures of conjugated polymer via self-assembly from mixed solvents, RSC Adv. 5 (2015) 76472−76475.
[19] J. Zhang, H. Yang, S. Xu, L. Yang, Y. Song, L. Jiang, Y. Dan, Dramatic enhancement of visible light photocatalysis due to strong interaction between TiO 2 and end-group functionalized P3HT, Appl. Catal. B Environ. 174 (2015) 193−202.
[20] C.-E. Cheng, F. Dinelli, C.-T. Yu, H.-W. Shih, Z. Pei, C.-S. Chang, F.S.-S. Chien, Influences of thermal annealing on P3HT/PCBM interfacial properties and charge dynamics in polymer solar cells, Jpn. J. Appl. Phys. 54 (2015) 122301.
[21] J.W. Jung, J.W. Jo, C.C. Chueh, F. Liu, W.H. Jo, T.P. Russell, A.K.Y. Jen, Fluoro-substituted n-type conjugated polymers for additive-free all-polymer bulk heterojunction solar cells with high power conversion efficiency of 6.71%, Adv. Mater 27 (2015) 3310−3317.
[22] J.H. Kim, S. Wood, J.B. Park, J. Wade, M. Song, S.C. Yoon, I.H. Jung, J.S. Kim, D.H. Hwang, Optimization and analysis of conjugated polymer side chains for high-performance organic photovoltaic cells, Adv. Funct. Mater 26 (2016) 1517−1525.
[23] P.R. Pratap, O. Dediu, G.U. Nienhaus, FTIR study of ATP-induced changes in Na+/K+-ATPase from duck supraorbital glands, Biophys. J. 85 (2003) 3707−3717.
[24] Y.-S. Wu, Y.-C. Wu, S.-W. Kuo, Thymine-and adenine-functionalized poly-styrene form self-assembled structures through multiple complementary hydrogen bonds, Polymers 6 (2014) 1827−1845.
[25] C. Kim, A. Facchetti, T.J. Marks, Polymer gate dielectric surface viscoelasticity modulates pentacene transistor performance, Science 318 (2007) 76−80.
[26] X. Zhao, Y. Zhao, Q. Ge, K. Butrouna, Y. Diao, K.R. Graham, J. Mei, Complementary semiconducting polymer blends: the influence of conjugation-break spacer length in matrix polymers, Macromolecules 49 (2016) 2601−2608.
[27] Z. Chen, P. Cai, J. Chen, X. Liu, L. Zhang, L. Lan, J. Peng, Y. Ma, Y. Cao, Low bandgap conjugated polymers with strong interchain aggregation and very high hole mobility towards highly efficient thick-film polymer solar cells, Adv. Mater. 26 (2014) 2586−2591.
[28] Y. Li, Y. Zou, Conjugated polymer photovoltaic materials with broad absorption band and high charge carrier mobility, Adv. Mater. 20 (2008) 2952−2958.

[29] J. Chen, H. Liu, W.A. Weimer, M.D. Halls, D.H. Waldeck, G.C. Walker, Non-covalent engineering of carbon nanotube surfaces by rigid, functional conjugated polymers, J. Am. Chem. Soc. 124 (2002) 9034—9035.

[30] W. Zhao, L. Feng, L. Xu, W. Xu, X. Sun, J. Hao, Chiroptical vesicles and disks that originated from achiral molecules, Langmuir 31 (2015) 5748—5757.

[31] M. Baghgar, E. Pentzer, A.J. Wise, J.A. Labastide, T. Emrick, M.D. Barnes, Cross-linked functionalized poly (3-hexylthiophene) nanofibers with tunable excitonic coupling, ACS Nano 7 (2013) 8917—8923.

[32] C. Rest, M.J. Mayoral, K. Fucke, J. Schellheimer, V. Stepanenko, G. Fernández, Self-assembly and (Hydro) gelation triggered by cooperative $\pi-\pi$ and unconventional C-H··· X hydrogen bonding interactions, Angew. Chem. Int. Ed. 53 (2014) 700—705.

[33] S.G. Hahm, Y. Rho, J. Jung, S.H. Kim, T. Sajoto, F.S. Kim, S. Barlow, C.E. Park, S.A. Jenekhe, S.R. Marder, High-performance n-channel thin-film field-effect transistors based on a nanowire-forming polymer, Adv. Funct. Mater. 23 (2013) 2060—2071.

[34] D. Tadaki, T. Ma, J. Zhang, S. Iino, A. Hirano-Iwata, Y. Kimura, R.A. Rosenberg, M. Niwano, Fabrication and characterization of p+-i-p+ type organic thin film transistors with electrodes of highly doped polymer, J. Appl. Phys. 119 (2016) 154503.

[35] S.A. Mollinger, B.A. Krajina, R. Noriega, A. Salleo, A.J. Spakowitz, Percolation, tie-molecules, and the microstructural determinants of charge transport in semicrystalline conjugated polymers, ACS Macro Lett. 4 (2015) 708—712.

[36] M. Hassan, Y.-C. Liu, K. ul Hasan, H. Butt, J.-F. Chang, R. Friend, Charge trap assisted high efficiency in new polymer-blend based light emitting diodes, Nano Energy 21 (2016) 62—70.

[37] C. Dyer-Smith, I.A. Howard, C. Cabanetos, A. El Labban, P.M. Beaujuge,

F. Laquai, Interplay between side chain pattern, polymer aggregation, and charge carrier dynamics in PBDTTPD: PCBM bulk-heterojunction solar cells, Adv. Energy Mater 5 (2015) 1401778.

[38] B. Kang, R. Kim, S.B. Lee, S.-K. Kwon, Y.-H. Kim, K. Cho, Side-chain-induced rigid backbone organization of polymer semiconductors through semi-fluoroalkyl side chains, J. Am. Chem. Soc. 138 (2015) 3679—3786.

[39] D. Khim, Y.R. Cheon, Y. Xu, W.-T. Park, S.-K. Kwon, Y.-Y. Noh, Y.-H. Kim, Facile route to control the ambipolar transport in semiconducting polymers, Chem. Mater. 28 (2016) 2287—2294.

[40] M. Baghgar, M.D. Barnes, Work function modification in P3HT H/J aggregate nanostructures revealed by kelvin probe force microscopy and photo-luminescence imaging, ACS Nano 9 (2015) 7105—7112.

[41] G. Wang, N. Persson, P.-H. Chu, N. Kleinhenz, B. Fu, M. Chang, N. Deb, Y. Mao, H. Wang, M.A. Grover, Microfluidic crystal engineering of π-conjugated polymers, ACS Nano 9 (2015) 8220—8230.

[42] S. Choulis, Y. Kim, J. Nelson, D. Bradley, M. Giles, M. Shkunov, I. McCulloch, High ambipolar and balanced carrier mobility in regioregular poly (3-hexylthiophene), Appl. Phys. Lett. 85 (2004) 3890—3892.

[43] J. Chan, X. Huang, A. Song, Nondestructive photolithography of conducting polymer structures, J. Appl. Phys. 99 (2006) 023710.

[44] X. Li, Y. Jiang, H. Tai, G. Xie, W. Dan, The fabrication and optimization of OTFT formaldehyde sensors based on Poly (3-hexythiophene)/ZnO composite films, Sci. China Tech. Sci. 56 (2013) 1877—1882.

[45] B. Tan, Y. Li, M.F. Palacios, J. Therrien, M.J. Sobkowicz, Effect of surfactant conjugation on structure and properties of poly (3-hexylthiophene) colloids and field effect transistors, Colloids Surf. A Physicochem. Eng. Asp. 488 (2016) 7—14.